The Journal of Physical Chemistry A

 VOLUME 102, NUMBER 29, JULY 16, 1998

FEATURE ARTICLE

Condensed-Phase Products in Heterogeneous Reactions: N_2O_5, $ClONO_2$, and HNO_3 Reacting on Ice Films at 185 K

Mark A. Zondlo, Stephen B. Barone,† and Margaret A. Tolbert*

Department of Chemistry and Biochemistry and Cooperative Institute for Research in Environmental Sciences, University of Colorado, Boulder, Colorado 80309

Received: November 10, 1997; In Final Form: April 21, 1998

Heterogeneous reactions are important in a wide variety of chemical processes. In many cases reactions on a surface will change both the physical and chemical characteristics of the surface, which in turn will change the surface reactivity toward further gas/surface collisions. As a case study of relevance to the atmosphere, we have investigated the reactions of the NO_y species $ClONO_2$, N_2O_5, and HNO_3 on thin ice films representative of water-ice polar stratospheric clouds (type II PSCs). Although these species are known to produce HNO_3 upon reacting with the ice surface, the phase, composition, and state of adsorption (physical versus chemical) of the surface reaction product are not known. These reactions were studied using a Knudsen cell reactor to probe heterogeneous reaction rates, mass spectrometry to identify gas-phase reactants and products, and FTIR reflection−absorption spectroscopy to probe the phase and composition of the condensed phase. Under ice frost point conditions at 185 K, each NO_y species reacted with ice to form a metastable supercooled H_2O/HNO_3 liquid layer. Although a crystalline 3:1 H_2O:HNO_3 hydrate is most thermodynamically stable under these conditions, a supercooled liquid with a composition slightly more dilute than 3:1 H_2O:HNO_3 continued to grow throughout the NO_y exposure period. This product composition is similar to that expected for liquid type Ib PSCs in the atmosphere. $ClONO_2$ and N_2O_5 reacted with the supercooled H_2O/HNO_3 liquid layer at 185 K with a reactive uptake coefficient of $\gamma = 0.003 \pm 0.002$ and $\gamma = 0.0007 \pm 0.0003$, respectively. These measured rate coefficients are about 2 orders of magnitude lower than the corresponding reaction rates on pure ice but are comparable to those measured on crystalline nitric acid trihydrate (NAT) or nitric acid dihydrate (NAD) surfaces representative of type Ia PSCs. HNO_3 reacted with the supercooled liquid layer with $\gamma > 0.02$. When H_2O vapor pressures were decreased to below the ice frost point, the supercooled H_2O/HNO_3 liquid layer became more concentrated in HNO_3 as H_2O preferentially desorbed. Only during desorption when stoichiometric ratios of 3:1 or 2:1 H_2O:HNO_3 were obtained did the supercooled liquid layer crystallize to NAT or NAD, respectively. These results suggest that water-ice particles in the polar stratosphere may be initially coated with a supercooled H_2O/HNO_3 liquid layer and that heterogeneous nucleation of NAT on ice from either the gas phase or the H_2O/HNO_3 supercooled liquid phase is slow. The implications of a supercooled H_2O/HNO_3 liquid layer on ice will be discussed in the context of polar ozone depletion.

Introduction

Heterogeneous reactions at the gas/surface interface play an important role in physical chemistry. Often, the rates of these reactions depend strongly on the physical and chemical characteristics of the condensed-phase surface.[1−3] Any product species that remain on the surface may alter the original

† Now at Department of Chemistry, George Washington University, 725 21st St. NW, Washington, DC 20236.

* To whom correspondence should be addressed.

S1089-5639(98)00131-5 CCC: $15.00
Published on Web 06/20/1998

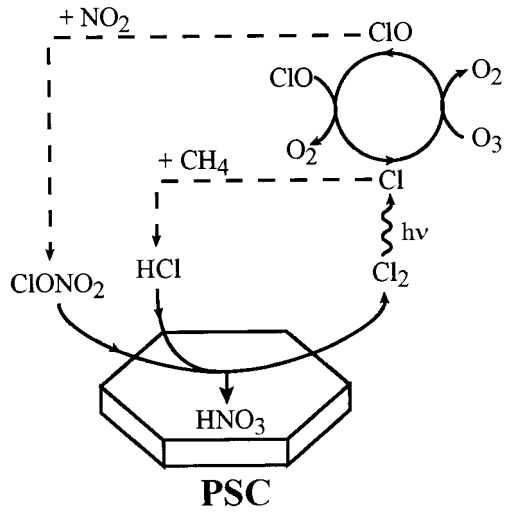

Figure 1. Heterogeneous reactions on polar stratospheric clouds convert photochemically inactive forms of chlorine like $ClONO_2$ and HCl into photolabile forms such as Cl_2. Once Cl_2 is photolyzed, atomic chlorine radicals catalytically deplete ozone. The cycle is terminated either when ClO reacts with NO_2 or by atomic chlorine reacting with CH_4. Although these reactions re-form reservoir chlorine, $ClONO_2$ and HCl will rapidly react to re-form Cl_2 in the presence of PSCs, thereby continuing the ozone depletion. This process causes the observed ozone "hole" each spring in the Antarctic stratosphere.

chemical reactivity of the surface toward further reaction. Furthermore, a surface-bound species on a dynamic surface may significantly impact physical properties such as desorption[4,5] and diffusion rates.[6] Thus, identifying the physical and chemical states of condensed-phase reaction products is essential for understanding the thermodynamics, rates, and mechanisms of gas/surface reactions.

One area where surface chemistry is increasingly showing its importance lies in atmospheric heterogeneous chemistry. The most dramatic example of surface chemistry in the atmosphere is the yearly formation of the Antarctic ozone "hole".[7,8] In the absence of heterogeneous chemistry, most inorganic chlorine in the stratosphere resides in the form of HCl or $ClONO_2$, molecules which neither significantly react with ozone nor are readily photolyzed by incoming solar radiation. However, in the presence of atmospheric surfaces such as polar stratospheric clouds (PSCs), heterogeneous reactions 1 and 2 convert $ClONO_2$and HCl into molecular chlorine (Cl_2), as depicted schematically in Figure 1:

$$ClONO_2(g) + HCl(g) \rightarrow Cl_2(g) + HNO_3(cond) \quad (1)$$

$$HCl(g) + HOCl(g) \rightarrow Cl_2(g) + H_2O(a) \quad (2)$$

where (g), (a), and (cond) refer to the gas, adsorbed (either physically or chemically), and condensed phases, respectively. Once formed, molecular chlorine is rapidly photolyzed by solar radiation at sunrise to produce atomic chlorine radicals. Atomic chlorine then attacks ozone molecules in the gas-phase catalytic cycle shown below with a net loss of two ozone molecules per cycle (reactions 3−6):[9]

$$2(Cl + O_3 \rightarrow ClO + O_2) \quad (3)$$

$$ClO + ClO + M \rightarrow (ClO)_2 + M \quad (4)$$

$$(ClO)_2 + h\nu \rightarrow ClO_2 + Cl \quad (5)$$

$$ClO_2 + M \rightarrow Cl + O_2 + M \quad (6)$$

where M is a third-body molecule. The above catalytic cycle continues until being terminated by the one of the following reactions:

$$ClO + NO_2 + M \rightarrow ClONO_2 + M \quad (7)$$

$$Cl + CH_4 \rightarrow HCl + CH_3 \quad (8)$$

The terminating reactions 7 and 8 re-form the photochemically inert forms $ClONO_2$ and HCl. However, in the presence of PSCs, as depicted schematically in Figure 1, heterogeneous reactions rapidly recycle chlorine back into photolabile forms and the catalytic ozone depletion cycle continues.

In addition to the heterogeneous reactions 1 and 2, several other important reactions occur on the surfaces of polar stratospheric cloud particles:

$$ClONO_2(g) + H_2O(a) \rightarrow HOCl(g) + HNO_3(cond) \quad (9)$$

$$N_2O_5(g) + H_2O(a) \rightarrow 2HNO_3(cond) \quad (10)$$

$$HNO_3(g) + H_2O(a) \rightarrow HNO_3(cond) + H_2O(a) \quad (11)$$

By producing condensed-phase HNO_3, reactions 9−11 remove the principal sources of NO_2 from the gas phase. As a result of these reactions, less NO_2 is available to deactivate chlorine monoxide back to $ClONO_2$ via reaction 7 and ozone loss is prolonged. While the overall reaction scheme in Figure 1 is now understood to be vital to the ozone hole formation, the details of what happens to the HNO_3 formed from reactions 1 and 9−11 are not clear. In this paper we examine the product HNO_3 formed on ice from reactions 9−11 to determine how the PSCs may be modified during the course of a reaction.

There are several types of PSCs that we will discuss in the present work. Type I PSCs form at temperatures around 193 K under typical stratospheric conditions and are primarily composed of H_2O and HNO_3 in either a crystalline phase (type Ia)[10−14] or liquid phase (type Ib).[11,10,15−17] Type II PSCs, on the other hand, consist of crystalline water-ice particles that form at or below the stratospheric ice frost point of ~188 K.[18] Type II PSCs occur regularly in the Antarctic mid-winter and are the dominant surface for chlorine activation during this time.[19] Although temperatures in the Arctic polar vortex are generally too warm for ice nucleation, type II PSCs have been observed in the Arctic during anomalously cold winters.[20−24]

Knowing the condensed-phase reaction products on ice surfaces is important in quantifying the rate of chlorine activation on type II PSCs. For example, the reaction of $ClONO_2$ on an ice surface has previously been shown to be very efficient with a reactive uptake coefficient $\gamma \geq 0.2$.[25,26] However, once an ice surface becomes sufficiently coated with the condensed-phase HNO_3 product, as depicted schematically in Figure 2, this reaction can no longer be characterized as occurring on an ice surface. Indeed, Hanson and Ravishankara suggested that $ClONO_2$ reacting with water-ice molecules formed a surface monolayer of nitric acid trihydrate (NAT).[25] The heterogeneous reaction rate of $ClONO_2$ over this NAT monolayer was $\gamma = 0.006$ at a relative humidity of 100% with respect to ice at 201 K,[25] about 2 orders of magnitude slower than the corresponding reaction on a "neat" ice surface. Therefore, to accurately model reactions occurring on type II

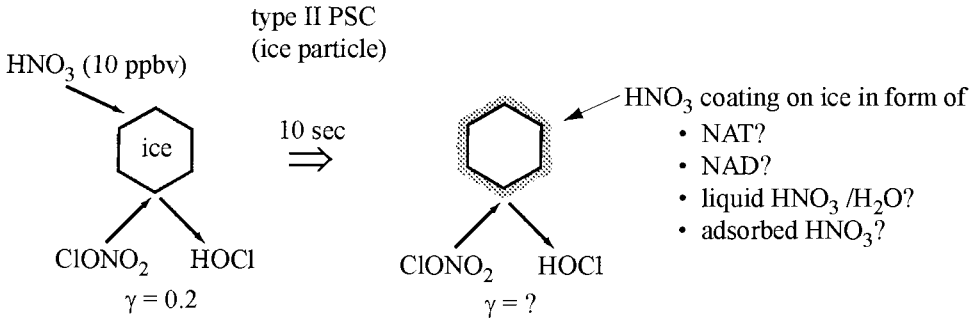

Figure 2. For polar stratospheric conditions of 10 ppbv HNO_3 at 60 mb, a type II PSC ice particle becomes coated with the resulting HNO_3 condensed-phase product in ~10 s according to gas kinetic theory (assuming $\gamma = 0.3$, 10^{15} ice sites cm^{-2}, and that the saturated surface has a 4:1 H_2O:HNO_3 composition). Because the heterogeneous reaction rates on ice and HNO_3/H_2O surfaces can vary by over an order of magnitude for certain species (e.g., $ClONO_2$ and N_2O_5), the goal of this work is to identify the condensed-phase products of these reactions and the corresponding heterogeneous reaction rates over this new surface.

PSCs, it is necessary to know the condensed-phase reaction products and how the reactive uptake coefficient changes on the corresponding new surface.

Despite the importance of the surface composition and phase on heterogeneous reaction rates, the condensed-phase products of reactions 9−11 have not been directly identified under stratospheric conditions, and there exists significant disagreement within the literature. For example, while reactions 9 and 10 are believed to form a monolayer of nitric acid trihydrate (NAT) on the ice surface,[25] reaction 11 has been suggested to form either a monolayer of NAT, a monolayer of nitric acid dihydrate (NAD), or a mixed hydrate composed of NAT and NAD.[27] In contrast, the reaction of $ClONO_2$ on ice was recently reported to form an amorphous H_2O/HNO_3 layer over the ice surface before crystallizing to a nitric acid hydrate.[26] In all of these experiments, the phase and composition of the resulting condensed-phase products were probed indirectly by measuring H_2O and HNO_3 partial pressures of the H_2O/HNO_3 adlayers. Although the condensed-phase products of reactions 9 and 10 have indeed been probed directly by infrared spectroscopy, these studies were done at temperatures and H_2O partial pressures well below those found in the stratosphere.[28−30]

In the present study we have investigated the reactions of N_2O_5, $ClONO_2$, and HNO_3 (reactions 9−11) on thin ice films at 185 K under stratospheric H_2O and NO_y reactant partial pressures. The experiments were conducted using a Knudsen cell reactor modified for Fourier transform infrared reflection−absorption spectroscopy (FTIR-RAS). FTIR-RAS is a highly sensitive probe of thin films while a Knudsen cell reactor allows for the determination of heterogeneous reaction rates. In combination, these techniques allow for in situ and simultaneous monitoring of gas-phase species and the condensed-phase thin film during the course of a heterogeneous reaction.

Experimental Section

The experimental setup consists of a Knudsen cell flow reactor and FTIR-RAS as shown schematically in Figure 3. The apparatus consists of two stainless steel chambers separated by a butterfly valve. The upper chamber houses an aluminum substrate upon which thin ice films are grown and an ionization gauge for pressure determination. The lower chamber contains an electron-impact quadrupole mass spectrometer, a Baratron capacitance manometer, an ionization gauge, two leak valves for the introduction of gases, and a gate valve leading to a turbomolecular pump. During experiments when the gate valve is closed, the chamber is pumped through a 0.17 cm^2 orifice drilled through the gate valve. NO_y reactant partial pressures in the chamber are determined by calibrating the ionization

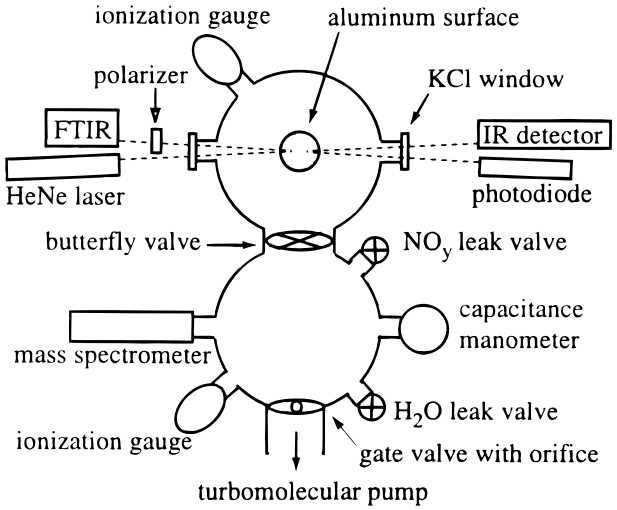

Figure 3. Experimental setup showing the Knudsen cell reactor and FTIR-RAS.

gauges and mass spectrometer signals to the Baratron capacitance manometer. Based on the reproducibility of the corresponding mass spectrometer signals, errors in pressure are estimated to be ±50% for $ClONO_2$ and N_2O_5 and ±20% for HNO_3. Water partial pressures are read directly by the capacitance manometer and are accurate to ±5%.

The substrate in the upper chamber is a 9.14 cm diameter optically flat aluminum disk (0.22 cm thick) in contact with an aluminum thermal break of the same diameter and 1.5 cm in length. The other end of the thermal break is connected to a Minco heater of similar diameter, followed by another aluminum thermal break in contact with a liquid nitrogen reservoir. Indium foil (Alpha Aesar, 0.127 mm thick) is placed on both sides of the heater to ensure good contact between the heater and the thermal breaks. The substrate is heated resistively against a liquid nitrogen reservoir, and the temperature is controlled by a Eurotherm temperature programmer to ±0.1 K. To probe the temperature directly, three copper−constantan thermocouples are attached to the outer edges of the aluminum surface using a thermally conductive epoxy. Temperature gradients across the surface as measured by the thermocouples are less than 0.5 K with the majority of gradient located near the edges of the substrate. The entire heating/cooling assembly is housed in a differentially pumped stainless steel sleeve with a poly(tetrafluoroethylene) seal between the sleeve and aluminum substrate. In this way the optically flat aluminum substrate is the only cold surface in the chamber.

Ice film thicknesses were determined by calibrating the integrated absorbance of the 3260 cm^{-1} OH stretch in the infrared ice spectra to film thicknesses derived from optical interference measurements using a helium−neon laser.[31] The first destructive and constructive interference fringes of the helium neon laser signal correspond to film thicknesses of 126 and 252 nm, respectively. Previous experiments have shown that the infrared spectra obtained in our setup can discern changes on the order of an ice bilayer spacing for films less than 100 nm thick,[31] consistent with the sensitivity of other FTIR-RAS studies.[32−34]

In a typical experiment the aluminum substrate is first cooled to ∼185 K, and a flow of H_2O is introduced into both chambers so that the pressure nears 1.03×10^{-4} Torr, the ice frost point at 185.0 K.[35] The flow of water is then gradually increased until ice nucleation occurs, usually at a pressure of $\sim 2.5 \times 10^{-4}$ Torr. Nucleation is observed in the infrared by the growth of a crystalline ice spectrum and simultaneously in the gas phase by a decrease in the H_2O partial pressure. By monitoring the integrated absorbance of the 3260 cm^{-1} OH stretch in crystalline hexagonal ice, the flow of water is then carefully adjusted to attain a desired film thickness of 10−50 nm.

The flow of water is then readjusted to maintain the ice film at the ice frost point. The ice frost point is experimentally determined when changes in the integrated absorbance of the 3260 cm^{-1} peak correspond to less than 1 nm of ice over a time of 2 min. The measured water pressure at this time of 1.06×10^{-4} ($\pm 3 \times 10^{-6}$) Torr is related to an ice frost point temperature of 185.0 (±0.1) K from known H_2O equilibrium ice vapor pressures.[35] Temperatures determined in this fashion agreed within 2 K of the direct, thermocouple measurements. However, because the errors in the thermocouple measurements are intrinsically large (±1 K) and may depend on the degree of contact with the aluminum surface, the temperatures reported here are those determined by the more precise ice equilibrium vapor pressure measurements.

After attaining the ice frost point, the butterfly valve between the two chambers is closed. A flow of NO_y reactant is introduced to the lower chamber and monitored by the mass spectrometer to ensure a steady flow. Under steady-state conditions the flow of molecules into the chamber equals the flow of molecules out of the chamber. For effusive loss of reactant molecules through an escape orifice, the flow F_o (molecules s^{-1}) of NO_y molecules out of the chamber is simply the product of the collision frequency with a surface (molecules cm^{-2} s^{-1}) and the area of the escape orifice A_h (cm^2):

$$F_o = \frac{P_0}{(2\pi mkT)^{0.5}} A_h \qquad \text{(I)}$$

where P_0 is the initial partial pressure before exposure, k is the Boltzmann constant, m is the molecular mass, and T is the temperature.

When the butterfly valve is opened, a decrease in the mass spectrometer signals is observed if NO_y uptake occurs on the ice film. The loss rate of molecules to the surface is given by the collision frequency with the geometric surface area of the film times the fraction (γ) of collisions that lead to reaction. Thus, the overall loss rate of molecules from the chamber is simply the sum of the loss rate by effusion and the loss rate to the surface:

$$F = \frac{P}{(2\pi mkT)^{0.5}} A_h + \frac{P}{(2\pi mkT)^{0.5}} A_s \gamma \qquad \text{(II)}$$

where P is the steady-state partial pressure during uptake of reactant NO_y molecules.

For steady-state conditions, conservation of mass requires that the flow of NO_y reactant molecules into the chamber must equal the combined loss rate of molecules to the surface and out the escape orifice. Because the flow of molecules into the chamber remains constant during the entire process, eq I can be set equal to eq II:

$$\frac{P_0}{(2\pi mkT)^{0.5}} A_h = \frac{P}{(2\pi mkT)^{0.5}} A_h + \frac{P}{(2\pi mkT)^{0.5}} A_s \gamma \qquad \text{(III)}$$

By solving eq III for the reactive uptake coefficient, γ, and by assuming that the mass spectrometer signals (S) are linear with respect to reactant partial pressure ($S \propto P$), the changes in the mass spectrometer signals before (S_0, ±5%) and after (S, ±5%) opening the butterfly valve can be expressed by the relation

$$\gamma = \frac{A_h (S_0 - S)}{A_s S} \qquad \text{(IV)}$$

where A_h is the area of the escape orifice (0.17 ± 0.01 cm^2)[36] and A_s is the geometric area of the ice film (72 ± 2 cm^2). When no additional changes in the mass spectrometer signals are observed, the butterfly valve is closed. Recovery of the signals to the previous levels before opening the butterfly valve is expected if the flows are constant throughout the duration of the experiment. For all experiments conducted in the present study, mass spectrometer signals were calibrated with respect to the capacitance manometer and found to be linear over the range of partial pressures used.

Infrared spectra were collected using a Nicolet Magna 550 spectrometer with a liquid nitrogen cooled mercury−cadmium−telluride detector. The infrared beam was passed through a polarizer, focused to near the center of the aluminum substrate, and reflected off the aluminum substrate at ∼84° from the surface normal. Spectra were obtained by the coaddition of 64 scans at 16 cm^{-1} resolution from 4000 to 650 cm^{-1}. Because FTIR-RAS on thin (<100 nm) water-ice films is essentially transparent to infrared radiation polarized perpendicular to the plane of incidence,[34,37] the infrared radiation was polarized parallel to the plane of incidence, resulting in an increase in the signal-to-noise ratio.

Reference spectra of amorphous H_2O/HNO_3 solutions were obtained by introducing stoichiometric partial pressures of H_2O and HNO_3 into the lower chamber. When stable flows were attained, the butterfly valve was opened to the upper chamber where the aluminum substrate was held at 140 K. By assuming unity sticking coefficients of HNO_3 and H_2O on the resulting H_2O/HNO_3 amorphous solutions at this temperature, FTIR-RAS reference spectra for 2:1, 3:1, and 4:1 H_2O:HNO_3 films were obtained for film thicknesses between 10 and 50 nm. The relative intensities of the OH stretch (∼3400 cm^{-1}) to the asymmetric nitrate (NO_3^-) stretches (∼1330, 1450 cm^{-1}) were then quantified over a baseline drawn from 3800 to 1070 cm^{-1}. By using the lower wavenumber NO_3^- peak, OH/NO_3^- peak intensity ratios of 0.8, 1.7, and 2.9 corresponded to film compositions of 2:1, 3:1, and 4:1 H_2O:HNO_3, respectively (Figure 4). The OH/NO_3^- ratios for the higher wavenumber NO_3^- peak were 0.9, 1.2, and 2.2 for film compositions of 2:1, 3:1, and 4:1 H_2O:HNO_3, respectively. Finally, as an additional check on our film compositions, reflection spectra of 2:1 and 3:1 H_2O:HNO_3 amorphous solutions were calculated[34] from known optical constants[38] assuming 10 nm thick films at incident

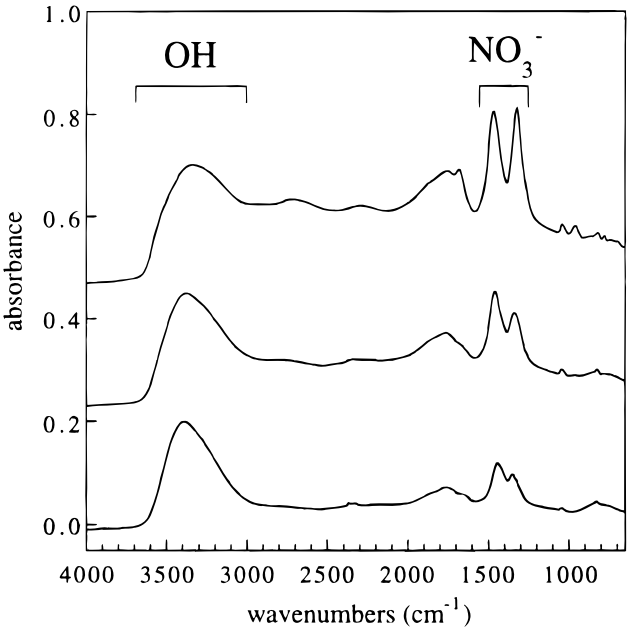

Figure 4. Reference FTIR-RAS spectra of amorphous H_2O:HNO_3 solutions at 140 K for compositions of 2:1 (top), 3:1 (middle), and 4:1 (bottom). The spectra were scaled and offset for clarity.

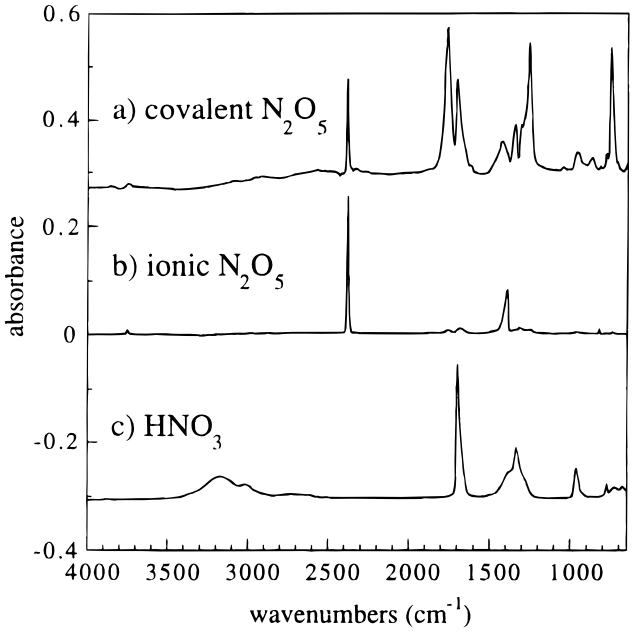

Figure 5. Deposition of (a) N_2O_5 at 105 K showing predominantly covalently bonded N_2O_5. (b) The same film annealed to 125 K showing ionic N_2O_5. (c) HNO_3 deposited at 105 K. The spectra have been offset and scaled for clarity.

infrared radiation 84° from surface normal. The OH/NO_3^- ratios for both NO_3^- peaks from the calculated spectra agreed to within 10% of those ratios determined experimentally.

$ClONO_2$ and N_2O_5 were synthesized and purified by previously described methods.[39,40] Both reactants were further purified before experiments by pumping on the sample for up to an hour while in a liquid nitrogen/ethanol bath held at −40 °C. N_2O_5 was also differentially pumped during use to minimize heterogeneous wall loss on the glass inlet line. HNO_3 vapor was obtained by making a 3 part (by volume) H_2SO_4 (98 wt %, Baxter) to 1 part HNO_3 (67 wt %, Baxter) bulb and drawing off the vapor which was >99.9% HNO_3.[41] The HNO_3/H_2SO_4 bulb and H_2O (HPLC grade, Aldrich) underwent several freeze, pump, and thaw cycles before use. Both bulbs were also submersed in a water-ice bath to ensure that the inlet line pressures on the backsides of leak valves were constant during the course of an experiment.

Results

Deposition of N_2O_5, $ClONO_2$, and HNO_3 at 105 K. To ensure that each reactant was entering the chamber in a pure form, $ClONO_2$, N_2O_5, and HNO_3 were individually deposited on the aluminum surface at 105 K. In all three cases, the deposited films suggested very pure sources of the reacting gases. The results of $ClONO_2$ deposition at 105 K have been previously discussed.[36] Figure 5 shows a spectrum of N_2O_5 deposited on the substrate at (a) 105 and (b) 125 K. By comparison to previous infrared studies of N_2O_5,[42,43] the seven fundamental modes of N_2O_5 that were within our detection range are clearly shown in the spectrum at 105 K. The two large peaks at 1765 and 1704 cm^{-1} correspond to the in-phase (ν_1) and out-of-phase (ν_{11}) NO_2 asymmetric stretches. The in-phase (ν_2) and out-of-phase (ν_{12}) NO_2 symmetric stretches are located at 1344 and 1257 cm^{-1}, respectively. The NO_2 bends are present at 753 cm^{-1} (in-phase, ν_3) and 782 cm^{-1} (out-of-phase, ν_{14}). Finally, the N−O−N asymmetric stretch (ν_{13}) corresponds to the peak at 868 cm^{-1}. Two other significant peaks at 2386 and 1425 cm^{-1} are assigned to ionic N_2O_5, i.e., $NO_2^+NO_3^-$. These ionic peaks can be seen more clearly upon annealing the film of N_2O_5 to 125 K where the film is almost completely converted to the ionic form (Figure 5b) with only traces of the covalent N_2O_5 peaks. The large peak at 2384 cm^{-1} has been assigned to the NO_2^+ asymmetric stretch while the broader band at 1396 cm^{-1} corresponds to the asymmetric NO_3^- stretch.[37]

The remaining peaks not assigned in Figure 5a to either the covalent or ionic structure of N_2O_5 are most likely trace amounts of HNO_3 or possible combination bands or overtones. For comparison, Figure 5c shows an infrared spectrum of HNO_3 deposited at 105 K. Based on previously assigned condensed-phase HNO_3 spectra,[44,43] the eight fundamental modes of HNO_3 can be readily identified. The largest two peaks at 1697 and 1336 cm^{-1} correspond to the NO_2 asymmetric (ν_2) and symmetric stretches (ν_3), respectively. The peak at 3170 cm^{-1} is the OH stretch (ν_1), and the shoulder at 1390 cm^{-1} is the H−O−N bend (ν_4). The NO_2 in-plane (ν_5) and out-of-plane (ν_8) bends are located at 965 and 773 cm^{-1}, respectively. Finally, the O−NO_2 stretch (ν_6) and bend (ν_7) are located at 722 and 707 cm^{-1}, respectively. Thus, it seems likely that only trace impurities of HNO_3 may be influencing the spectrum in Figure 5a and that the N_2O_5 flow into the chamber is very pure.

It is unclear whether the trace impurity of HNO_3 in the N_2O_5 spectrum results from heterogeneous decomposition of N_2O_5 on the chamber walls, a remaining impurity from the N_2O_5 synthesis, or from reaction of N_2O_5 with ice at 105 K. Because the base pressure in our chamber of $\sim 2 \times 10^{-8}$ Torr is significantly higher than the ice frost point pressure at 105 K ($<10^{-10}$ Torr), a very thin (<5 nm) ice film was present before deposition of N_2O_5. Previous studies have shown a rapid reaction of $ClONO_2$ on ice at temperatures around 100 K,[36,45,46] and a similar efficient reaction between N_2O_5 and ice might be producing the HNO_3 impurity observed at 105 K. Because of significant shifts in peak positions from the highly ionic environment and from the FTIR-RAS technique, it is not entirely possible to unambiguously identify all of the minor peaks in Figure 5a. Nonetheless, deposition of $ClONO_2$, N_2O_5, and HNO_3 at 105 K all showed the observed fundamentals within the range of detection and only trace amounts of impurities.

Reaction of N_2O_5 on Ice at 185 K. After attaining an ice film in dynamic equilibrium as described previously, the

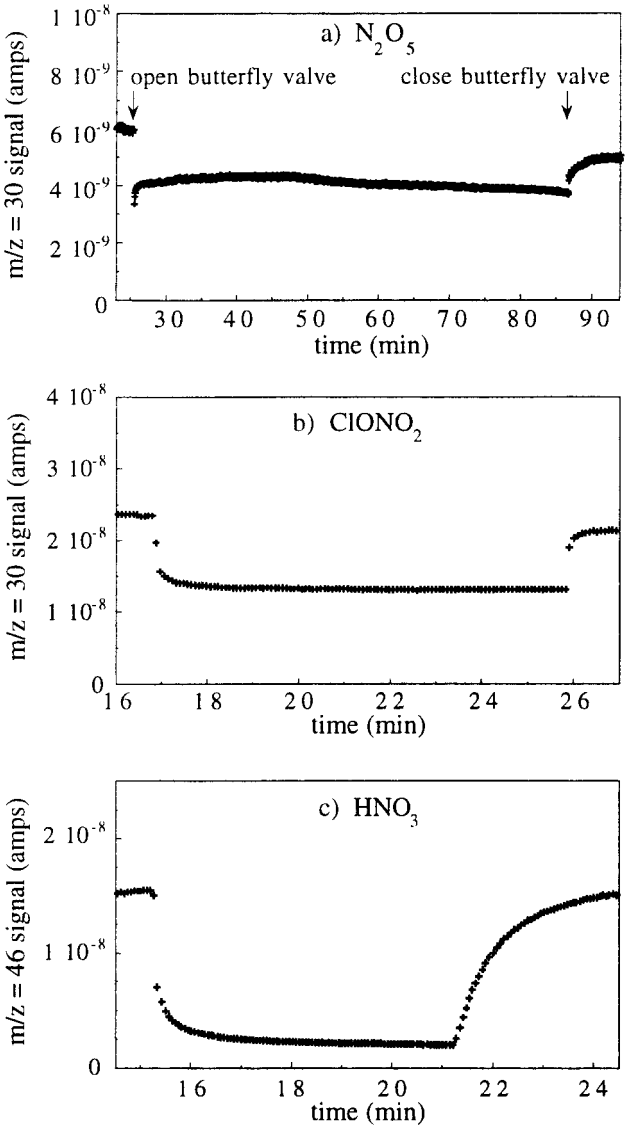

Figure 6. Mass spectrometer signals upon opening the butterfly valve between the two chambers and exposing the 185 K ice film to a flow of (a) N_2O_5, (b) $ClONO_2$, and (c) HNO_3.

butterfly valve between the chambers was closed. A reactant flow rate of 3×10^{14} molecules s^{-1} N_2O_5 was then introduced to the lower chamber as determined by the calibrated $m/z = 30$ (NO^+) and $m/z = 46$ (NO_2^+) mass spectrometer signals. The mass spectrum of N_2O_5 showed fragmentation between the $m/z = 30$ and $m/z = 46$ signals in the ratio of ~70:1. No parent ion was observed for N_2O_5 ($m/z = 108$), but a highly pure flow of N_2O_5 was entering the chamber as shown in Figure 5 by the low-temperature deposition on aluminum. The flow of N_2O_5 was adjusted to achieve stable signals in the mass spectrometer for the time scale of the experiment before opening the butterfly valve.

When the butterfly valve was opened, the flow of N_2O_5 was exposed to the ice film. A precipitous drop was initially observed in the mass spectrometer signals followed by a rapid rise to a steady-state value for the remainder of the exposure time. Figure 6a shows the initial drop of the $m/z = 30$ signal and the partial recovery to a steady-state value within the first few minutes of a typical experiment. As will be discussed later in more detail, this behavior shortly after opening the butterfly valve is related to uptake on two different surfaces. The $m/z = 30$ signal indicated that the steady-state N_2O_5 partial pressure over the thin film was 8×10^{-6} Torr. Upon closing the butterfly

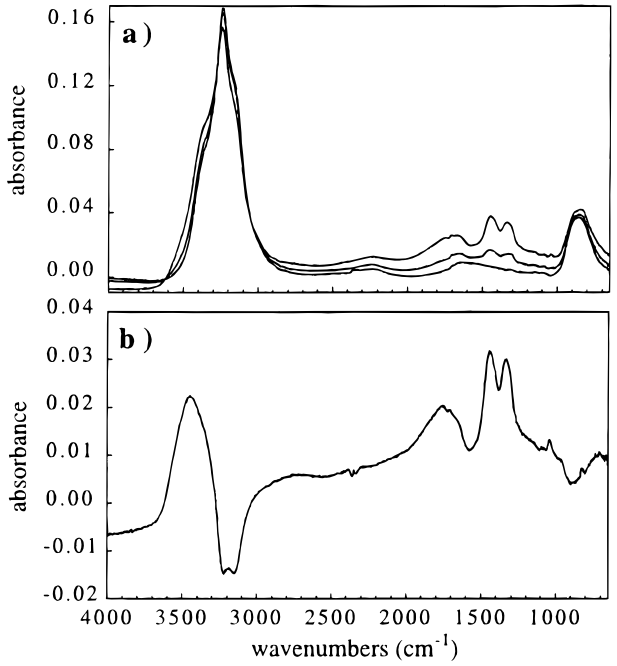

Figure 7. (a) Infrared spectra of the N_2O_5 reacting with an ice film at 185 K. The lowermost spectrum is the initial ice film, followed by spectra taken at $t = 1$ min and $t = 3$ min after exposure to N_2O_5. (b) Difference spectrum resulting from the subtraction of the initial ice spectrum from the spectrum at $t = 3$ min. The double peaks in the nitrate region indicate the formation of a supercooled liquid H_2O/HNO_3 layer.

valve and thereby isolating the thin film from the flow of N_2O_5, the mass spectrometer signals recovered to nearly their levels before exposing the N_2O_5 flow to ice.

Because the initial uptake changed rapidly and was not sufficiently time-resolved in the mass spectrometer signals, we report an uptake coefficient for N_2O_5 over the saturated surface during the time of the steady-state uptake. In addition, the uptake coefficients calculated from eq IV for the $m/z = 46$ signals were a factor of 2 greater than those of the $m/z = 30$ signals. We attribute this discrepancy in the uptake coefficient to a slight impurity of HNO_3 in the N_2O_5 flow. HNO_3 fragments almost equally (~2:1) between $m/z = 30$ and $m/z = 46$ and has a large uptake coefficient ($\gamma > 0.3$)[27] on HNO_3-saturated surfaces. Given the 70:1 ratio of the m/z 30:46 mass spectrometer signals for N_2O_5, any HNO_3 impurity in the N_2O_5 flow would interfere more with the $m/z = 46$ signal than the $m/z = 30$ signal. Therefore, only the $m/z = 30$ signal was used to calculate an average uptake coefficient of $\gamma = 0.0007 \pm 0.0003$ for N_2O_5 over the saturated surface. This reported uptake coefficient is the mean value of 19 experiments conducted using N_2O_5 steady-state partial pressures of 7×10^{-7} to 1×10^{-5} Torr.

When N_2O_5 was exposed to the ice film, several changes also occurred in the infrared spectra. Figure 7a shows the spectrum of the initial ice film before exposure, followed by spectra taken 1 and 3 min after exposure. The most noticeable changes include the growth of a pair of peaks around 1445 and 1335 cm^{-1} and a new peak around 1700 cm^{-1}. These peaks have been previously identified as the splitting of the doubly degenerate asymmetric NO_3^- stretch and the H_3O^+ bend, respectively.[47,48]

To gain a better understanding of the changes in the condensed phase, a difference spectrum shown in Figure 7b was obtained by subtracting the initial ice spectrum from the spectrum taken 3 min after exposure. In addition to the

pronounced NO_3^- and H_3O^+ absorbance peaks, it becomes clearer that the OH region consists of a broad peak, shifted to a higher energy (~3450 cm^{-1}) than that of crystalline ice. The lack of sharp absorption features indicative of NAT or NAD in the OH and NO_3^- regions suggests that the reaction of N_2O_5 with the ice surface forms an amorphous H_2O/HNO_3 solution. Reference spectra of amorphous H_2O/HNO_3 solutions help identify the peak at ~3450 cm^{-1} as the amorphous OH stretch. We attribute the large negative peak at ~3200 cm^{-1} to the loss of crystalline H_2O ice superimposed with the growth of the amorphous OH stretch. Despite the loss of crystalline ice, the difference spectrum clearly shows the ionization of HNO_3 on the surface into NO_3^- and H_3O^+. The ratios of the OH/NO_3^- peaks for this spectrum were 1.3 and 1.2 for the 1335 and 1445 cm^{-1} peaks, respectively. Based on the reference spectra in Figure 4, an amorphous solution of composition slightly less than 3:1 H_2O:HNO_3 is obtained. However, because the loss of crystalline ice in the OH stretching region decreases the OH/NO_3^- ratios, it seems likely that the true composition of this film is closer to 3:1 H_2O:HNO_3. In addition, the loss of crystalline ice in the infrared spectra made it difficult to identify whether the supercooled H_2O/HNO_3 liquid composition changed systematically with N_2O_5 partial pressures.

While it is not possible to differentiate between an amorphous solid and supercooled liquid using infrared spectroscopy, the phase of this H_2O/HNO_3 layer is most likely a supercooled liquid. The glass temperatures for H_2O/HNO_3 solutions are near 155 K,[49] well below the present experimental temperature of 185 K. In addition, the composition of this amorphous solution responded quickly to changes in the partial pressures of H_2O and HNO_3, thereby suggesting a more mobile liquid phase. Nonetheless, the possibility of forming amorphous solids of H_2O/HNO_3 at stratospheric temperatures, as has been recently reported,[50] cannot be ruled out from the infrared spectra alone. Because the N_2O_5 reaction on ice appears to form a supercooled H_2O/HNO_3 solution, the reported saturated uptake efficiency of $\gamma = 0.0007 \pm 0.0003$ for N_2O_5 corresponds to uptake on a supercooled liquid layer.

Reaction of $ClONO_2$ on Ice at 185 K. To study reaction 9, a $ClONO_2$ flow of 4×10^{14} molecules s^{-1} was introduced to the lower chamber and monitored by the $m/z = 30$ (NO^+), $m/z = 46$ (NO_2^+), $m/z = 35$ ($^{35}Cl^+$), and $m/z = 37$ ($^{37}Cl^+$) mass spectrometer signals. Again, while no parent ions ($m/z = 97$, 99) were observed for $ClONO_2$, a highly pure flow of $ClONO_2$ was entering the chamber as shown by spectra taken during deposition at 105 K.[36] Because of possible interferences with the reaction product HOCl, which has been shown to desorb from ice after saturating at coverages of a few percent,[26,51,52] the chlorine fragments were not used in calculating the reactive uptake coefficient for this reaction.

After attaining a stable $ClONO_2$ flow into the lower chamber, the butterfly valve separating the chambers was opened and an ice film was exposed to $ClONO_2$ (Figure 6b). A drop was immediately seen in all mass spectrometer signals, followed by a gradual flattening of the signal with time. The mass spectrometer signals indicated that the steady-state $ClONO_2$ partial pressure over the surface was 4×10^{-6} Torr. No other changes were observed for the duration of the experiment until the butterfly valve was closed at which point the signals recovered to near their previous values before opening. By using the $m/z = 30$ and $m/z = 46$ signals with eq IV for 13 experiments, an average reactive uptake coefficient of $\gamma = 0.003 \pm 0.002$ was calculated for $ClONO_2$ on the saturated ice layer.

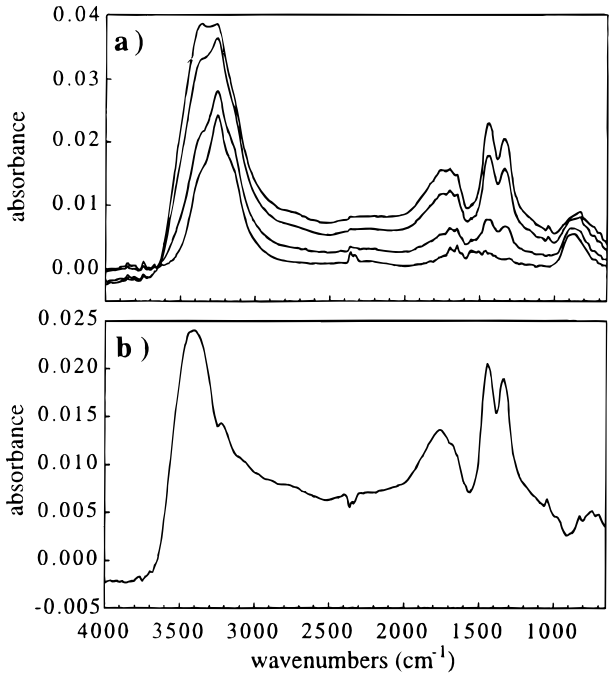

Figure 8. (a) Infrared spectra for an ice film exposed to $ClONO_2$ at 185 K. The lowermost spectrum is the initial ice spectrum, followed by spectra taken every minute thereafter. (b) Difference spectrum obtained by subtracting the ice spectrum from the one at $t = 3$ min, indicating the formation of a supercooled H_2O:HNO_3 liquid of composition slightly greater than 3:1.

These experiments were conducted over a range of $ClONO_2$ steady-state partial pressures from 6×10^{-7} to 3×10^{-5} Torr.

Infrared spectra of the ice film when exposed to $ClONO_2$ are shown in Figure 8a, with the lowermost spectrum being the initial ice film before exposure, followed by spectra taken every minute thereafter for the first 3 min. The appearance of NO_3^- asymmetric stretches (1440 and 1335 cm^{-1}) and the H_3O^+ bend (1700 cm^{-1}) shows the ionization of the reaction product HNO_3. A broadening of the OH stretch is also observed, but it remains difficult to identify this change unambiguously from the spectra alone. Infrared spectra taken throughout the $ClONO_2$ exposure showed that the NO_3^- and OH peaks continued to grow, consistent with the continuous uptake observed by the mass spectrometer.

A difference spectrum in Figure 8b obtained by subtracting the ice spectrum from the spectrum at $t = 3$ min clearly shows the formation of a H_2O/HNO_3 supercooled liquid with only a minor loss of crystalline ice observed at 3300 cm^{-1}. The ratios of the intensities of the OH stretch to the asymmetric NO_3^- stretches are 1.8 (1335 cm^{-1}) and 1.6 (1440 cm^{-1}). Based on the amorphous reference spectra at 140 K (Figure 4), the composition of this supercooled liquid is slightly greater than 3:1 H_2O:HNO_3. The composition of this layer did not change significantly with time and remained in a supercooled liquid phase throughout the exposure time. In addition, no variation in composition was noted over the range of $ClONO_2$ partial pressures studied.

Reaction of HNO_3 on Ice at 185 K. In an analogous experiment to those described above, a nitric acid flow of 2.2×10^{14} molecules s^{-1} was added to the lower chamber. When stable signals were achieved in the mass spectrometer for the $m/z = 30$ (NO^+), $m/z = 46$ (NO_2^+), and $m/z = 63$ (HNO_3^+) signals, the butterfly valve was opened to the ice film and large drops were observed in all the signals, followed by a gradual leveling of the signals with time (Figure 6c). The mass

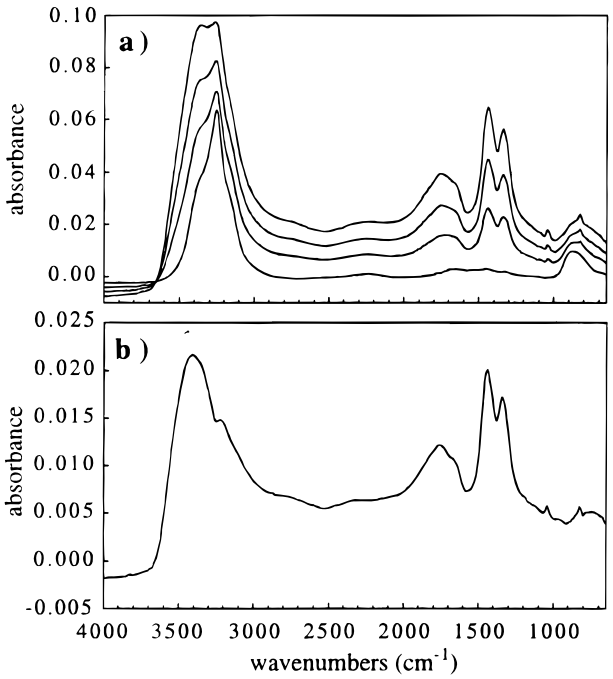

Figure 9. (a) Infrared spectra upon exposing HNO_3 to ice at 185 K. The lowermost spectrum is the initial ice film, followed by spectra taken every ~3 min. (b) Difference spectrum obtained by subtracting the spectrum at $t = 6$ min from the spectrum at $t = 9$ min, indicating the formation of a supercooled ~3:1 H_2O:HNO_3 liquid.

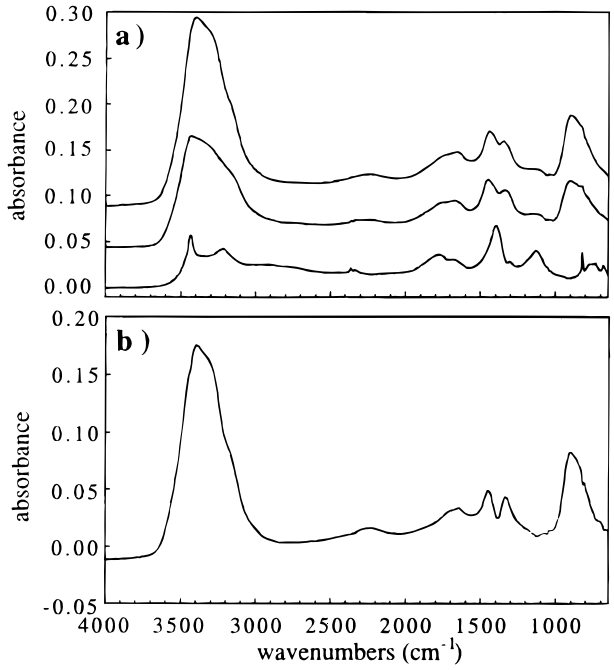

Figure 10. (a) Infrared spectra of the H_2O/HNO_3 film upon a decrease of $P(H_2O)$ to below the ice frost point at 185 K. The uppermost spectrum corresponds to a supercooled H_2O/HNO_3 liquid on ice while the lowermost spectrum corresponds to α-NAT. The spectra were offset for clarity. (b) A difference spectrum obtained by subtracting the α-NAT spectrum from the uppermost spectrum. By comparing the OH region (~3400 cm^{-1}) to the NO_3^- region (~1330, 1440 cm^{-1}), it can be seen that water molecules preferentially desorbed from the film.

spectrometer signals indicated that the HNO_3 partial pressure over the surface was 5.3×10^{-7} Torr. After closing the butterfly valve, all of the signals recovered to their previous values before exposure to the ice film. An average uptake coefficient of $\gamma > 0.02$ was calculated using the signals of the $m/z = 30$ and $m/z = 46$ fragments. The $m/z = 63$ signal was not sufficiently (~10 times) above background levels to accurately calculate γ by eq IV. Because reactive uptake coefficients greater than 0.02 cannot be measured in the present Knudsen cell reactor,[36] we report a lower limit for the uptake of HNO_3 over the thin film.

Infrared spectra of the condensed phase showed the immediate uptake of HNO_3 on the film by the growth of the asymmetric NO_3^- and the H_3O^+ peaks, consistent with the growth of a supercooled H_2O/HNO_3 liquid on ice (Figure 9a). Like the results of N_2O_5 and $ClONO_2$ uptake experiments, the supercooled liquid layer never crystallized to a hydrate during the time scale of the experiments (up to 3 h) while at ice frost point vapor pressures. Similar to the subtraction spectra for $ClONO_2$ and N_2O_5 uptake on ice, a small loss of crystalline H_2O ice is observed at ~3240 cm^{-1} (Figure 9b). The OH/NO_3^- ratios of 1.8 (1330 cm^{-1}) and 1.4 (1440 cm^{-1}) indicate a supercooled liquid composition of slightly greater than 3:1 H_2O:HNO_3.

Unlike the results for N_2O_5 and $ClONO_2$ reacting with ice to form a supercooled H_2O/HNO_3 liquid layer, the composition of this layer was clearly dependent on the initial reactant HNO_3 flows. For steady-state partial pressures from 1.2×10^{-7} to 9.6×10^{-6} Torr, the composition of the resulting supercooled liquid layer ranged from almost 4:1 to 2:1 H_2O:HNO_3, respectively. Nonetheless, even when the supercooled liquid grew in at the stoichiometric ratio of 3:1 H_2O:HNO_3, crystallization to NAT was not observed while at the ice frost point.

H_2O/HNO_3 Layer upon Decrease of P_{H_2O}. After closing the butterfly valve and thereby isolating the thin films from the flow of NO_y, there were no further increases in absorbances or any other changes in the infrared spectra. The flow of water was then decreased so that the relative humidity was less than the ice frost point, followed by opening the butterfly valve. As shown in Figure 10a, the overall absorbance of the spectra began to decrease, signaling a desorption of the film. In particular, a large decrease in the ratio of the OH to NO_3^- absorbances was observed, indicating that the supercooled HNO_3/H_2O liquid layer was becoming more concentrated in HNO_3. A subtraction spectrum (Figure 10b) taken of this process shows the preferential desorption of water molecules (OH region near ~3350 cm^{-1}) over HNO_3 molecules (NO_3^- peaks at ~1340 and 1450 cm^{-1}). Because water molecules were desorbing from both the crystalline ice underlayer and the supercooled liquid overlayer, it was difficult to quantify the rate and relative amounts of the desorption for each species from the infrared spectra.

When compositions of the supercooled liquid reached 3:1 H_2O:HNO_3, the thin film sometimes crystallized into NAT as shown in the final spectrum in Figure 10a. Although the relative intensities of the NAT peaks differ slightly from the reference spectra taken by transmission spectroscopy,[53] the NAT spectrum observed Figure 10a agrees well with previous FTIR-RAS spectra of NAT.[36] In the absence of NAT crystallization at compositions of 3:1 H_2O:HNO_3, the supercooled H_2O/HNO_3 liquid layer continued to preferentially lose H_2O over HNO_3 and therefore became more concentrated in HNO_3. NAD crystallization was always observed to occur after attaining a composition of 2:1 H_2O:HNO_3. For faster desorption rates (lower relative humidities), NAD crystallization was more common than NAT. This is consistent with previous work which showed a higher nucleation barrier for NAT than NAD from 3:1 and 2:1 H_2O:HNO_3 supercooled liquids, respectively.[54] Faster desorption rates resulted in a shorter time near the 3:1 composition for NAT to crystallize. Therefore, when NAT did not crystallize, H_2O continued to desorb until a 2:1 composition was reached, at which point NAD crystallized.

Discussion

The present infrared study shows that under ice frost point conditions the NO_y species $ClONO_2$, N_2O_5, and HNO_3 react on ice to form a supercooled liquid layer of composition near 3:1 H_2O:HNO_3. Previous studies have reported measurements of rapid reaction for $ClONO_2$ ($\gamma \geq 0.2$),[26,25] N_2O_5 ($\gamma = 0.024$),[25] and HNO_3 ($\gamma \geq 0.2$)[27] on ice. Because these species react so efficiently with pure ice surfaces, our initial ice films should "saturate" to a monolayer of supercooled ~3:1 H_2O:HNO_3 on the order of a minute. For example, with a $ClONO_2$ partial pressure of 4×10^{-6} Torr, the chamber contains $\sim 10^{15}$ molecules of $ClONO_2$ in the ~10 L volume. Because loss of $ClONO_2$ by effusion through the pump-out orifice is very slow relative to uptake by the surface, it can be assumed that almost all of the $ClONO_2$ molecules initially in the chamber react rapidly with the ice surface to produce adsorbed HNO_3 and HOCl. Therefore, almost immediately after exposing the ice film to a flow of $ClONO_2$, up to ~10% of the ice surface sites are covered by the reaction products of $ClONO_2$, assuming 1.15×10^{15} sites cm^{-2} for an ice surface[55] and a geometric ice film surface area of 72 cm^2. It appears that this coverage is sufficient to decrease the uptake of $ClONO_2$ by the film to a rate much slower than that over pure ice. For the reaction of N_2O_5 on ice (Figure 6a), a much larger uptake was observed initially than at later times. Unfortunately, the time resolution of our mass spectrometer was insufficient to quantify this larger uptake. Because N_2O_5 reacts with a pure ice surface about 10 times slower than $ClONO_2$, it seems likely that for N_2O_5 we were measuring a much larger uptake on ice initially before the ice sites became coated with sufficient amounts of HNO_3 to slow the reaction.

The subtraction spectra of the product adlayers of N_2O_5, $ClONO_2$, and HNO_3 on ice all show the ionization of HNO_3 on the surface into NO_3^- and H_3O^+. Nonetheless, the region of the amorphous OH stretch in the subtraction spectra are not completely identical to that of the amorphous 3:1 H_2O:HNO_3 spectrum shown in Figure 4. Specifically, all of the subtraction spectra contain a negative peak located around ~3200 cm^{-1}. This dip is attributed to the loss of the crystalline ice OH peak superimposed with the growth of the amorphous OH stretch.

The loss of crystalline ice may result either from ice desorption at H_2O partial pressures slightly below the ice frost point or from the incorporation of surface and near-surface ice molecules into the supercooled liquid. Even when additional experiments were conducted at H_2O partial pressures slightly greater (~10%) than the ice frost point, some loss of crystalline ice was still observed. Furthermore, throughout the duration of the exposure time, a slow loss of crystalline ice was observed during the uptake of the NO_y species. Therefore, it seems likely that water-ice molecules at the ice/liquid interface were converted from the environment of a crystalline ice lattice to one of a supercooled liquid. Nonetheless, H_2O-ice molecules desorbing from the surface at relative humidities slightly less than 100% may also play a significant role in the observed loss of crystalline ice.

The formation of a supercooled liquid on ice and the loss of crystalline ice with time can be better understood by examining the H_2O/HNO_3 phase diagram shown in Figure 11. In this figure the NAD/NAT and NAT/ice coexistence curves define the thermodynamic stability regions for these crystalline hydrates.[13,14] Specifically, NAD is thermodynamically stable in the upper, left corner of the diagram while ice is most stable in the lower, right corner. Between these two regions, NAT is the thermodynamically stable form of H_2O/HNO_3. To relate

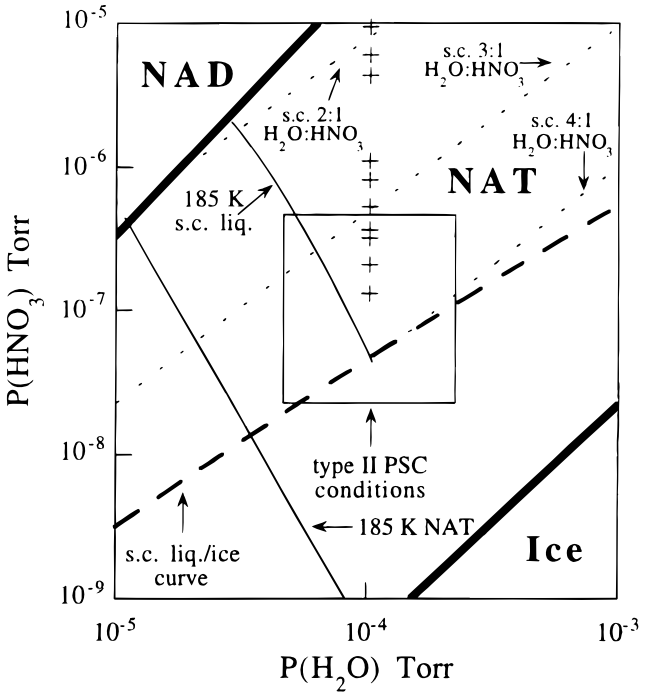

Figure 11. HNO_3/H_2O phase diagram from Worsnop et al. (1993) showing the NAD, NAT, and "ice" stability regions. In addition, the ice−H_2O/HNO_3 supercooled liquid coexistence curve and supercooled liquid 2:1, 3:1, and 4:1 H_2O:HNO_3 composition curves are shown from Tabazadeh et al. (1994). Plus symbols (+) represent experimental conditions for HNO_3 uptake at 185 K. For reference, the 185 K NAT and supercooled H_2O/HNO_3 liquid isotherms are also shown. All experiments conducted at the ice frost point resulted in the formation of a supercooled liquid rather than NAT. The box outlines the range of polar stratospheric conditions expected when type II PSCs are present.

the H_2O/HNO_3 phase diagram in Figure 11 to the experimental conditions used in the present study, the 185 K NAT isotherm has also been included. Conditions above and to the right of this line at 185 K can result in NAT growth. Conversely, NAT is expected to evaporate when below and to the left of this isotherm. Finally, a box outlining the range of stratospheric conditions for type II PSCs has been included in Figure 11 for reference (1−5 ppmv H_2O, 0.5−10 ppbv HNO_3 at 60 mb).

Because NAT was not observed in the present study under ice frost point conditions, it was necessary to superimpose on Figure 11 a metastable phase diagram for supercooled H_2O/HNO_3 liquids. By using the thermodynamic model of Tabazadeh et al.,[56] the ice-supercooled liquid coexistence curve, the 185 K supercooled liquid isotherm, and the 2:1, 3:1, and 4:1 supercooled H_2O/HNO_3 liquid compositional curves were added to the NAT region of Figure 11. The "ice"-supercooled H_2O/HNO_3 liquid coexistence curve was solved analytically by equating H_2O vapor pressures of ice[35] and supercooled H_2O/HNO_3 solutions[56] over 1 K increments. For H_2O and HNO_3 partial pressures located above the ice/supercooled liquid coexistence curve, ice is unstable with respect to a supercooled liquid, and consequently, ice begins to melt in the presence of a supercooled liquid. In contrast, for conditions below the coexistence curve, a supercooled liquid is unstable with respect to ice and therefore begins to desorb from the ice surface. For all conditions shown in Figure 11, a supercooled liquid is unstable with respect to NAT.

To help better understand the curves in Figure 11, we will discuss supercooled H_2O/HNO_3 liquids in the context of the phase rule:

$$F = C - P + 2 \quad \text{(V)}$$

where F is the number of intensive variables that can be changed independently without disturbing the number of phases at equilibrium, C is the number of components, and P is the number of phases at equilibrium. A supercooled H_2O/HNO_3 liquid in equilibrium with its vapor contains two components (H_2O and HNO_3) and two phases (vapor and liquid). Therefore, there are two independent variables within the four variables of H_2O and HNO_3 partial pressures, composition, and temperature.[57,58] For example, when at a specific temperature, such as being located on the 185 K supercooled liquid isotherm shown in Figure 11, there is only one remaining degree of freedom. Of the remaining three variables, one more can be chosen independently before fixing the other two. Thus, each point along the 185 K supercooled liquid isotherm is defined by a unique set of H_2O partial pressure, HNO_3 partial pressure, and composition. In analogous reasoning, along a curve of constant composition, each point has a different temperature determined by the unique H_2O and HNO_3 partial pressures. Finally, when a supercooled liquid is in equilibrium with ice and vapor ($C = 2$, $P = 3$), only one degree of freedom exists. If one chooses a specific temperature for ice and supercooled liquid to be in equilibrium, the remaining variables of composition and HNO_3 and H_2O partial pressures are fixed. Therefore, each point along the ice/liquid coexistence curve also contains a unique set of composition, temperature, and H_2O and HNO_3 partial pressures.

Selected experimental HNO_3 partial pressures during the times of steady-state HNO_3 uptake are also shown in Figure 11 as plus signs. For those experiments conducted at the 185 K ice frost point, the experimental H_2O/HNO_3 partial pressures were always greater than the ice/supercooled liquid coexistence curve. Indeed, the formation and growth of a supercooled liquid on ice was always observed in the infrared spectra under these conditions. In addition, the composition of the supercooled liquid was observed to vary from ~2:1 to almost 4:1 H_2O:HNO_3 as the HNO_3 partial pressure decreased from $\sim 10^{-5}$ to 10^{-7} Torr. Unfortunately, due to the uncertainties in film composition ($\pm$20%) and HNO_3 partial pressures ($\pm$20%), it is difficult to precisely quantify the supercooled liquid composition as a function of HNO_3 partial pressure. Nonetheless, the observed dependence of composition on HNO_3 partial pressure is consistent with the binary H_2O/HNO_3 liquid solution from Tabazadeh et al.[56] Finally, the slow loss of crystalline ice observed in the infrared spectra also agrees with the expected melting of ice when above the ice/liquid coexistence curve. Only when located on the coexistence curve would ice and supercooled H_2O/HNO_3 liquid layers exist at equilibrium.

In contrast to experiments at the ice frost point, when the partial pressures of H_2O were decreased to below the ice frost point, the supercooled liquid composition became more concentrated in HNO_3. Again, this observation is consistent with the expected behavior of supercooled H_2O/HNO_3 liquids shown in Figure 11 as H_2O partial pressures decrease. Because H_2O partial pressures were changing rapidly during this process, we were unable to identify the location on the phase diagram where NAT or, more commonly, NAD crystallized. However, observations of the infrared spectra of supercooled liquids immediately before crystallization suggested that NAD or NAT only crystallized when stoichiometric ratios of 2:1 or 3:1 H_2O:HNO_3 liquids were attained, respectively.

Although the conditions in this study were located well to the right and above the 185 K NAT isotherm, the growth of NAT (or any other crystalline hydrate) on ice was not observed under ice frost point conditions, in apparent disagreement with previously reported studies. By measuring H_2O and HNO_3 partial pressures of the resulting condensed-phase products in flow tube experiments, Hanson and Ravishankara suggested the formation of a monolayer of NAT on ice when ice was exposed to either N_2O_5 or $ClONO_2$.[25] In addition, Hanson suggested that a monolayer of either a mixed hydrate of NAT/NAD or NAD formed on the ice surface from the reaction of HNO_3 on ice.[27] In both studies the presence of a supercooled H_2O/HNO_3 liquid layer was ruled out because the HNO_3 vapor pressures needed to support such a liquid were significantly greater than those observed experimentally. While monolayer coverages of either NAT or NAD appear to be in disagreement with what we observed in the present study, the flow tube results can possibly be explained by differences in experimental conditions.

The flow tube studies noted that their H_2O partial pressures were accurate to $\pm$50%. Therefore, it is possible that relative humidities in those experiments were significantly below 100%. We found that a supercooled H_2O/HNO_3 liquid layer on ice only formed when at the ice frost point. When slightly below the ice frost point, water desorbed from the film to form a more concentrated solution. A supercooled liquid may have formed initially in the flow tube studies, followed by the desorption of water to form a more concentrated solution and eventual crystallization to a hydrate. Indeed, recent work by Oppliger et al. showed that $ClONO_2$ reacting with ice at 188 K produced a condensed-phase product with a higher HNO_3 vapor pressure than that of either NAT or NAD, and it was suggested that an amorphous H_2O/HNO_3 solution had initially formed on the ice surface.[26] Over time, however, the measured vapor pressure decreased to that of NAT. Thus, we believe that the flow tube studies were likely conducted under subsaturated conditions with respect to ice which resulted in crystalline hydrates forming over ice.

The results of the present study also indicate that direct heterogeneous nucleation of NAT on ice from the gas phase is unlikely to occur. In addition, heterogeneous nucleation of NAT on ice from a supercooled H_2O/HNO_3 liquid also appears to be unlikely unless near the stoichiometric ratios of H_2O/HNO_3 crystalline hydrates. Our longest experiment showed the presence of a supercooled liquid for 3 h before ending the experiment without observing NAT. However, the crystalline ice OH peak in the infrared spectra was difficult to identify after 1 h due to melting of the underlying ice film in the presence of the supercooled liquid. The last 2 h of data suggest that homogeneous nucleation of NAT from the liquid is a slow process, particularly at nonstoichiometric ratios of H_2O/HNO_3. These results are consistent with the conclusion of Koop et al. that heterogeneous nucleation of NAT on ice from liquid H_2O/HNO_3 solutions is slow.[59] We also note that laboratory aerosols composed of binary H_2O/HNO_3 solutions have not been observed to nucleate NAT homogeneously from the liquid.[60] Although NAT is the most thermodynamically stable form of H_2O and HNO_3 under most stratospheric conditions, our results along with those studies noted above suggest that the nucleation of NAT in the stratosphere is strongly hindered.

Although the reactive uptake coefficients on supercooled H_2O/HNO_3 liquids have not been measured directly in the past, some insight into these reactions can be obtained by comparing their rates to those on H_2O/HNO_3 crystalline phases. For $ClONO_2$ on supercooled ~3:1 H_2O:HNO_3 liquid, our value of $\gamma = 0.003 \pm 0.002$ is comparable to that on a NAT surface of 0.006 ± 0.002 at a relative humidity of 100% at 201 K.[25] N_2O_5 likewise reacts very similarly at the ice frost point whether on a

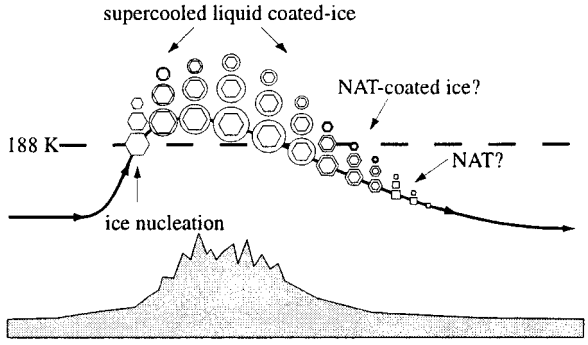

Figure 12. For a typical lee wave type II PSC, ice particles may be rapidly coated with a supercooled H_2O/HNO_3 liquid under lower stratospheric conditions. As the air parcel descends and warms adiabatically, H_2O is preferentially desorbed, resulting in a more HNO_3 concentrated supercooled liquid. Eventually, NAT or NAD may crystallize over the ice surface to slow the ice desorption rate (refs 74, 75) and prolong the lifetime of ice crystals (ref 76).

supercooled ~3:1 H_2O:HNO_3 liquid surface ($\gamma = 0.0007 \pm 0.0003$) or on a NAD/NAT surface (0.0006 ± 0.0003).[25] Although significant changes in reactivity occur on solid versus liquid phases for many reactions,[61] this does not appear to be the case for $ClONO_2$, N_2O_5, and HNO_3 reacting on H_2O/HNO_3 surfaces. As noted above, however, it is not entirely possible to compare these studies to the present one because the condensed-phase products in the former experiments were not known accurately. Furthermore, the experimental conditions of temperature, water vapor pressure, and HNO_3 partial pressure were slightly different in all of these studies which could lead to different condensed-phase products. Nonetheless, even if the previous studies examined the reactions on NAT or NAD films, recent studies suggest that the surfaces of crystalline hydrates in the presence of stratospheric H_2O partial pressures may be somewhat liquidlike in nature,[36,62] in which case some agreement between the reactivities on crystalline hydrates and supercooled liquid solutions should be expected.

Atmospheric Implications

Based on the results of the present study, when stratospheric ice clouds form (type II PSCs), they will be rapidly coated with HNO_3 to produce a supercooled H_2O/HNO_3 liquid over the ice surface. However, the environment in which the cloud forms and the dynamics of the air parcel will play a major role in the chemical and physical state of an individual ice particle. To help understand this process, we attempt below to describe conditions expected in the formation and dissipation of a type II PSC. In addition, we will examine the time scales necessary for a supercooled liquid to coat ice under stratospheric conditions and to reach equilibrium HNO_3 partial pressures between the gas and condensed phases.

Figure 12 shows a schematic of a lee wave-induced ice cloud in the stratosphere (type II PSC). Lee wave clouds form when air parcels are forced to rise due to flow over a topographic constraint such as a mountain range. As an air parcel in this trajectory begins to rise, the air expands and cools adiabatically. After supersaturating a few degrees below the ice frost point temperature of 188 K, ice nucleation is thought to occur on preexisting $HNO_3/H_2SO_4/H_2O$ aerosols. The composition of these aerosols at the time of ice nucleation is currently not known because under conditions of rapid cooling, gas-phase partial pressures may not be in equilibrium with certain sizes of preexisting aerosol particles.[63,64] To further complicate matters, ice nucleation appears to occur readily at these temperatures whether in binary solutions of H_2SO_4/H_2O or in binary solutions of HNO_3/H_2O.[65,66] Nonetheless, very recently Carslaw et al. modeled an observed lee wave type II PSC and showed that ice nucleation occurred <4 K below the ice frost point on liquid aerosols.[23,24]

It is unclear how much HNO_3 is buried into the bulk of ice during the rapid growth process or the state of the preexisting aerosol after ice nucleation. However, solubility measurements of HNO_3 in ice at warmer temperatures suggest maximum concentrations on the order of ppm.[67] With type II PSC ice volume densities[68] of ~1 μm^3 cm^{-3} and typical polar stratospheric vortex HNO_3 mixing ratios of 10 ppbv at 60 mb,[69] the maximum amount of HNO_3 incorporated in the bulk of ice is $\sim 10^4$ molecules cm^{-3}, an amount that is negligible compared to initial gas-phase HNO_3 concentrations of 2.4×10^{10} molecules cm^{-3}.

Shortly after the nucleation of ice particles, the uptake of the gas-phase HNO_3 onto the ice surfaces is expected to rapidly coat the ice particles with a supercooled H_2O/HNO_3 liquid. As shown on the H_2O/HNO_3 phase diagram in Figure 11, initial HNO_3 partial pressures of 4.5×10^{-7} Torr are significantly above the ice/liquid coexistence curve. With typical ice surface area densities for type II PSCs ranging from 10^1 to 10^3 μm^2 cm^{-3},[18,70] a supercooled ~4:1 H_2O:HNO_3 liquid layer on ice can be rapidly formed. For example, by assuming $\gamma = 0.3$ for HNO_3 on ice[27] and 1.15×10^{15} H_2O molecules cm^{-2} on an ice surface,[55] a surface coating of 4:1 H_2O:HNO_3 on ice will occur in ~10 s according to gas kinetic theory. This time scale is much shorter than the individual ice particle lifetimes of 10^3–10^5 s.[18] Because the number of HNO_3 molecules per volume (2.4×10^{10} molecules cm^{-3}) is greater than the number of ice surface sites per volume (10^8–10^{10} sites cm^{-3}), multilayer coverages of a 4:1 H_2O:HNO_3 liquid will form over ice surfaces. By assuming a monolayer spacing of 3 Å, a supercooled liquid of composition 4:1 H_2O:HNO_3 will initially grow at a rate of ~3 nm min^{-1} according to gas kinetic theory.

As HNO_3 is taken up by ice particles, the HNO_3 partial pressure will decrease until reaching equilibrium somewhere along the ice/liquid coexistence curve. Based on the ice/liquid coexistence curve shown in Figure 11, a supercooled H_2O/HNO_3 liquid may exist at ambient HNO_3 partial pressures as low as 4.6×10^{-8} Torr (~1 ppbv at 60 mb) at 185 K with an expected composition of ~4:1 H_2O:HNO_3.[56] The rate of change in gas-phase HNO_3 partial pressure as a function of time can be estimated by gas kinetic theory. The number of HNO_3 molecules lost to ice surfaces per cm^3 per second, dn/dt (cm^{-3} s^{-1}), is simply the product of the collision frequency with a surface z (cm^{-2} s^{-1}), the fraction of collisions that react with the surface γ (unitless), and the surface area density A (cm^2 cm^{-3}):

$$dn/dt = -z\gamma A \qquad \text{(VI)}$$

By substituting the ideal gas law, $n = PV/kT$ (where $V = 1$ cm^3 in this case), substituting for the collision frequency $z = P/(2\pi mkT)^{0.5}$, and then rearranging in terms of the HNO_3 partial pressure, P, we find

$$\frac{dP}{dt} = -\frac{P\gamma AkT}{(2\pi mkT)^{0.5}} \qquad \text{(VII)}$$

By integrating eq VII with respect to pressure (from initial pressure P_i to final pressure P_f) and time (from 0 to t), the integrated form can then be solved to determine the time in which a final pressure is attained from an initial pressure:

$$t = \ln\left(\frac{P_i}{P_f}\right)\frac{\sqrt{2\pi mkT}}{\gamma AkT} \qquad \text{(VIII)}$$

By using eq VIII with an initial HNO_3 partial pressure of 4.5×10^{-7} Torr and a final partial pressure of 4.6×10^{-8} Torr (ice−supercooled liquid equilibrium at 185 K), the time scale to achieve equilibrium between the gas and condensed phases of HNO_3 ranges from 10^4 to 10^2 s for ice surface area densities of $A = 10^1$ μm^2 cm^{-3} and $A = 10^3$ μm^2 cm^{-3}, respectively. This calculation suggests that, in either shorter-lived PSCs or low surface area density PSCs, the gas-phase HNO_3 mixing ratios may never reach equilibrium with respect to the condensed phase on the ice surfaces. In contrast, for longer lived ice clouds or higher ice surface area densities, equilibrium between the gas and condensed phases occurs on a short time scale relative to the ice particle lifetime. By dividing the number of molecules lost from the gas phase by the number of ice surface sites, an average equilibrium thickness of the 4:1 H_2O/HNO_3 supercooled liquid over ice ranges between ~3 ($A = 10^3$ μm^2 cm^{-3}) and 300 nm ($A = 10^1$ μm^2 cm^{-3}). Thus, relative to the average size of type II ice particles (order of micrometers), the thickness of a supercooled liquid over ice is expected to be quite thin.

We caution, however, that the above calculations have assumed that negligible amounts of gas-phase HNO_3 are taken up by the preexisting aerosols before ice nucleation. However, even if the preexisting aerosols are primarily composed of H_2O/HNO_3, it is very possible that the preexisting aerosols will remain a liquid on the surface of the newly formed ice particle.[23,71] Thus, the calculations in this section may still remain applicable to PSC chemistry. In addition, we have not included the production of condensed-phase HNO_3 by other NO_y species reacting on the surface such as $ClONO_2$ and N_2O_5. Because these species react efficiently to form HNO_3 on pure ice surfaces, N_2O_5 and $ClONO_2$ will be particularly important in determining the time scales needed to coat newly formed ice surfaces with HNO_3. Furthermore, we have not addressed the possible melting of the underlying ice surface into the supercooled liquid when under conditions of supercooled liquid growth. Clearly, more accurate modeling of the uptake of NO_y over solid ice[72] and liquid H_2O/HNO_3 surfaces[73] would be helpful to accurately determine the behavior of supercooled liquids on ice surfaces. Nonetheless, to first order, ice particles appear to be quickly coated with a supercooled H_2O/HNO_3 liquid.

As an air parcel inside a type II PSC stops rising near the cloud midpoint, the particle is expected to slow or stop its growth. In this region the supercooled liquid-coated ice particle may experience minor fluctuations in relative humidity around the ice frost point. It seems that these short-lived perturbations would only cause slight changes in the film composition and not induce nucleation to a crystalline hydrate. However, once air begins to descend inside the lee wave cloud, it warms adiabatically and the relative humidity begins to decrease. Based on our results, H_2O molecules will preferentially desorb over HNO_3 molecules during the descent, possibly resulting in a highly concentrated H_2O/HNO_3 liquid[63,64] layer around the ice particle. Eventually, when a 3:1 or 2:1 H_2O:HNO_3 supercooled liquid ratio is attained, NAT or NAD may crystallize over the ice surface.

Laboratory studies have shown that NAT-coated ice may evaporate at temperatures as high as 8 K above the ice frost point.[74,75] Indeed, ice particles from type II PSCs have been observed at distances far downwind of lee wave clouds, well beyond the expected lifetime of ice particles under these conditions.[22] It has been proposed that a NAT coating formed over these ice particles and thereby slowed the ice evaporation rate.[76] Furthermore, another recent field study has observed the presence of nitrate ions on type II PSC ice particles existing in subsaturated environments.[68] As described above and shown in Figure 12, a supercooled liquid over ice particles might be a precursor in producing a NAT coating over ice and the subsequent decrease in ice desorption rates. This could also provide a mechanism to help explain observations of small NAT particles far downwind of lee wave ice clouds.[23]

All of the above calculations have assumed that type II PSC conditions were within the metastability region of supercooled H_2O/HNO_3 liquids. In contrast, when the initial conditions are expected to be below the ice−supercooled liquid coexistence curve but still sufficient to grow NAT, previous studies of the HNO_3/ice system have suggested that HNO_3 will coat ice particles up to a maximum coverage of one monolayer.[77,78] Thus, the possibility of nucleating NAT heterogeneously from the gas phase on ice still remains unlikely even when below the ice/liquid coexistence curve.

The presence of a supercooled 4:1 H_2O:HNO_3 liquid layer on stratospheric ice particles may have several effects on the chemistry occurring in the polar stratosphere. Because the time scale for coating pure ice surfaces is short under stratospheric conditions, type II PSCs may be most appropriately modeled with uptake coefficients on HNO_3-saturated surfaces such as a supercooled liquid, NAT, or NAD. The uptake coefficients for $ClONO_2$ and N_2O_5 on a supercooled liquid layer are about 2 orders of magnitude slower than their respective rates on pure ice surfaces. Therefore, significant decreases in the activation rates of reservoir species of chlorine within type II PSCs may be expected.

A supercooled liquid coating on ice may also affect heterogeneous reaction rates for other species. For example, numerous studies have shown that, under stratospheric conditions, HCl uptake is limited to a coverage of one monolayer on the ice surface[52,79] with very little bulk diffusion and solubility in the bulk of ice.[80,81] However, in the presence of a supercooled H_2O/HNO_3 liquid, HCl taken up by the surface might undergo diffusion into the bulk volume of the liquid layer. Depending on the solubility of HCl in a binary supercooled H_2O/HNO_3 solution and the thickness of the supercooled H_2O/HNO_3 layer, different amounts of HCl may be taken up by a liquid-coated ice particle than that expected by a pure ice particle. Furthermore, trace amounts of other species such as H_2SO_4 might also be incorporated into the solution. A highly ionic layer containing H_2SO_4, HNO_3, and HCl has been proposed produce nitrosyl sulfuric acid[82] along with a large number of other ionic reactions.[83]

Because the stratosphere can support and sustain a supercooled H_2O/HNO_3 liquid layer on ice, studies of PSC composition and phase might be more complex than identifying a one-phase particle composed of pure ice, NAT, or a supercooled liquid solution. For example, infrared extinction studies of polar stratospheric clouds did not match any of the simple systems such as NAT, NAD, ice, or supercooled liquid solutions.[84] In addition, field studies of PSCs in the Arctic have shown areas of clouds containing mixed particles phases and geometries.[85,86] While a mixture of different phase particles within a certain area of a cloud may help to explain these observations, a supercooled ~4:1 H_2O:HNO_3 liquid layer on ice may also need to be considered.

Finally, we note that the ~3:1 H_2O:HNO_3 composition of the supercooled liquid observed in the present study is similar

to that expected when background binary H_2SO_4/H_2O aerosols cool to 185 K under lower stratospheric conditions.[15,16,56,87] When temperatures cool gradually, background H_2SO_4/H_2O aerosols pick up increasing amounts of HNO_3 and H_2O, eventually resulting in a ternary solution of $H_2O/H_2SO_4/HNO_3$ at type I PSC temperatures. Below temperatures of ~191 K, enough HNO_3 and H_2O have condensed on the aerosols that their composition is primarily H_2O and HNO_3 with only trace amounts of H_2SO_4. Therefore, the uptake coefficients reported in the present work over a supercooled H_2O/HNO_3 liquid may also be applicable to liquid type Ib PSC aerosols for temperatures below ~191 K when the solutions are essentially composed of supercooled H_2O/HNO_3 solutions. The expected composition of these aerosols at a temperature of 188 K is ~4:1 H_2O:HNO_3,[15,16,56,87] consistent with that observed experimentally in the present study of ~3:1 H_2O:HNO_3.

Acknowledgment. The authors thank B. Berland, L. Goldfarb, and the NOAA Aeronomy Laboratory for their assistance in the $ClONO_2$ and N_2O_5 syntheses. We also thank A. Tabazadeh for sending us the code for the binary H_2O/HNO_3 system, T. Onasch and R. Bianco for helpful discussions, M. Robinson for invaluable work on the instrument design and construction, and two anonymous reviewers for helpful comments and suggestions on the manuscript. M.A.Z. gratefully acknowledges support from NASA Earth Systems Science and Global Change Fellowships. M.A.T. gratefully acknowledges support as an NSF Young Investigator and a Camille-Dreyfus teacher−scholar. This research was funded by NSF grant ATM-9711969 and NASA grant SA98-0005.

References and Notes

(1) Nathanson, G. M.; Davidovits, P.; Worsnop, D. R.; Kolb, C. E. *J. Phys. Chem.* **1996**, *100*, 13007.

(2) Rettner, C. T.; Auerbach, D. J.; Tully, J. C.; Kleyn, A. W. *J. Phys. Chem.* **1996**, *100*, 13021.

(3) Molina, M. J.; Molina, L. T.; Golden, D. M. *J. Phys. Chem.* **1996**, *100*, 12888.

(4) Chen, J.-P.; Crutzen, P. J. *J. Geophys. Res.* **1994**, *99*, 18847.

(5) Chen, J.-P.; Crutzen, P. J. *J. Geophys. Res.* **1996**, *101*, 23037.

(6) George, S. M.; Livingston, F. E. *Surf. Rev. Lett.* **1997**, *4*, 771.

(7) Solomon, S.; Garcia, R. R.; Rowland, F. S.; Wuebbles, D. J. *Nature* **1986**, *321*, 755. For a comprehensive review of polar ozone chemistry, see: *Scientific Assessment of Ozone Depletion: 1994*; World Meteorological Organization, Global Ozone Research and Monitoring Project, Report No. 37.

(8) Farman, J. C.; Gardiner, B. G.; Shanklin, J. D. *Nature* **1985**, *315*, 207.

(9) Molina, L. T.; Molina, M. J. *J. Phys. Chem.* **1987**, *91*, 433.

(10) Toon, O. B.; Browell, E. V.; Kinne, S.; Jordan, J. *Geophys. Res. Lett.* **1990**, *17*, 393.

(11) Browell, E. V.; Butler, C. F.; Ismail, S.; Robinette, P. A.; Carter, A. F.; Higdon, N. S.; Toon, O. B.; Schoeberl, M. R.; Tuck, A. F. *Geophys. Res. Lett.* **1990**, *17*, 385.

(12) Toon, O. B.; Hamill, P.; Turco, R. P.; Pinto, J. *Geophys. Res. Lett.* **1986**, *13*, 1284.

(13) Hanson, D.; Mauersberger, K. *Geophys. Res. Lett.* **1988**, *15*, 855.

(14) Worsnop, D. R.; Fox, L. E.; Zahniser, M. S.; Wofsy, S. C. *Science* **1993**, *259*, 71.

(15) Tabazadeh, A.; Turco, R. P.; Drdla, K.; Jacobson, M. Z.; Toon, O. B. *Geophys. Res. Lett.* **1994**, *21*, 1619.

(16) Carslaw, K. S.; Luo, B. P.; Clegg, S. L.; Peter, T.; Brimblecombe, P.; Crutzen, P. J. *Geophys. Res. Lett.* **1994**, *21*, 2479.

(17) Del Negro, L. A.; Fahey, D. W.; Donnelly, S. G.; Gao, R. S.; Keim, E. R.; Wamsley, R. C.; Woodbridge, E. L.; Dye, J. E.; Baumgardner, D.; Gandrud, B. W.; Wilson, J. C.; Jonsson, H. H.; Loewenstein, M.; Podolske, J. R.; Webster, C. R.; May, R. D.; Worsnop, D. R.; Tabazadeh, A.; Tolbert, M. A.; Kelly, K. K.; Chan, K. R. *J. Geophys. Res.* **1997**, *102*, 13255.

(18) Turco, R.; Toon, O. B.; Hamill, P. *J. Geophys. Res.* **1989**, *94*, 16493.

(19) Vömel, H.; Hofmann, D. J.; Oltmans, S. J.; Harris, J. M. *Geophys. Res. Lett.* **1995**, *22*, 2381.

(20) Hansen, G.; Hoppe, U.-P. *Geophys. Res. Lett.* **1997**, *24*, 131.

(21) Vömel, H.; Rummukainen, M.; Kivi, R.; Karhu, J.; Turunen, T.; Kyrö, E.; Rosen, J.; Kjome, N.; Oltmans, S. *Geophys. Res. Lett.* **1997**, *24*, 795.

(22) Deshler, T.; Peter, T.; Müller, R.; Crutzen, P. *Geophys. Res. Lett.* **1994**, *21*, 1327.

(23) Carslaw, K. S.; Wirth, M.; Tsias, A.; Luo, B. P.; Dörnback, A.; Leutbecher, M.; Volkert, H.; Renger, W.; Bacmeister, J. T.; Peter, T. *J. Geophys. Res.* **1998**, *103*, 5785.

(24) Carslaw, K. S.; Wirth, M.; Tsias, T.; Luo, B. P.; Dörnbrack, A.; Leutbecher, M.; Volkert, H.; Renger, W.; Bacmeister, J. T.; Reimer, E.; Peter, T. *Nature* **1998**, *391*, 675.

(25) Hanson, D. R.; Ravishankara, A. R. *J. Geophys. Res.* **1991**, *96*, 5081.

(26) Oppliger, R.; Allanic, A.; Rossi, M. J. *J. Phys. Chem. A* **1997**, *101*, 1903.

(27) Hanson, D. R. *Geophys. Res. Lett.* **1992**, *19*, 2063.

(28) Horn, A. B.; Koch, T.; Chesters, M. A.; McCoustra, M. R. S.; Sodeau, J. R. *J. Phys. Chem.* **1994**, *98*, 946.

(29) Sodeau, J. R.; Horn, A. B.; Banham, S. F.; Koch, T. G. *J. Phys. Chem.* **1995**, *99*, 6258.

(30) Koch, T. G.; Banham, S. F.; Sodeau, J. R.; Horn, A. B.; McCoustra, M. R. S.; Chesters, M. A. *J. Geophys. Res.* **1997**, *102*, 1513.

(31) Zondlo, M. A.; Onasch, T. B.; Warshawsky, M. S.; Tolbert, M. A.; Mallick, G.; Arentz, P.; Robinson, M. S. *J. Phys. Chem. B* **1997**, *101*, 10887.

(32) Graham, J. D.; Roberts, J. T. *J. Phys. Chem.* **1994**, *98*, 5974.

(33) Schaff, J. E.; Roberts, J. T. *J. Phys. Chem.* **1994**, *98*, 6900.

(34) Greenler, R. G. *J. Chem. Phys.* **1966**, *44*, 310. For calculated spectra, a correction was made in eq A8. The final argument was changed to $[n_3 - ik_3]\{E_3^+ \exp[(-2\pi d/\lambda)(\beta_3 + i\alpha_3 \cos \phi_3)]\}$.

(35) Marti, J.; Mauersberger, K. *Geophys. Res. Lett.* **1993**, *20*, 363.

(36) Barone, S. B.; Zondlo, M. A.; Tolbert, M. A. *J. Phys. Chem. A* **1997**, *101*, 8643.

(37) Horn, A. B.; Banham, S. F.; McCoustra, M. R. S. *J. Chem. Soc., Faraday Trans.* **1995**, *91*, 4005.

(38) Toon, O. B.; Tolbert, M. A.; Koehler, B. G.; Middlebrook, A. M.; Jordan, J. *J. Geophys. Res.* **1994**, *99*.

(39) Davidson, J. A.; Cantrell, C. A.; Shetter, R. E.; McDaniel, A. H.; Calvert, J. G. *J. Geophys. Res.* **1987**, *92*, 10921.

(40) Davidson, J. A.; Viggiano, A. A.; Howard, C. J.; Dotan, I.; Fehsenfeld, F. C.; Albritton, D. L.; Ferguson, E. E. *J. Chem. Phys.* **1978**, *68*, 2085.

(41) Taleb, D.-E.; Ponche, J.-L.; Mirabel, P. *J. Geophys. Res.* **1996**, *101*, 25967.

(42) Hisatsune, I. C.; Devlin, J. P.; Wada, Y. *Spectrochim. Acta* **1962**, *18*, 1641.

(43) Mélen, F.; Herman, M. *J. Phys. Chem. Ref. Data* **1992**, *21*, 831.

(44) McGraw, G. E.; Bernitt, D. L.; Hisatsune, I. C. *J. Chem. Phys.* **1965**, *42*, 237.

(45) Berland, B. S.; Tolbert, M. A.; George, S. M. *J. Phys. Chem. A* **1997**, *101*, 9954.

(46) Bianco, R.; Hynes, J. T. *J. Phys. Chem. A* **1998**, *102*, 309.

(47) Ritzhaupt, G.; Devlin, J. P. *J. Phys. Chem.* **1991**, *95*, 90.

(48) Ferriso, C. C.; Hornig, D. F. *J. Chem. Phys.* **1955**, *23*, 1464.

(49) Ji, K.; Petit, J. C.; Négrier, P.; Haget, Y. "Complémentarité des méthodes de diffraction des RX et d'analyse énérgetique dans la caracterisation des équilbres HNO_3−H_2O"; XIXièmes Journées d'étude des équilibres entre phases, 1993, Barcelona, Spain.

(50) Tabazadeh, A.; Toon, O. B. *J. Geophys. Res.* **1996**, *101*, 9071.

(51) Hanson, D. R. *J. Phys. Chem.* **1995**, *99*, 13059.

(52) Hanson, D. R.; Ravishankara, A. R. *J. Phys. Chem.* **1992**, *96*, 2682.

(53) Koehler, B. G.; Middlebrook, A. M.; Tolbert, M. A. *J. Geophys. Res.* **1992**, *97*, 8065.

(54) Tisdale, R. T.; Middlebrook, A. M.; Prenni, A. J.; Tolbert, M. A. *J. Phys. Chem. A* **1997**, *101*, 2112.

(55) Eisenberg, D.; Kauzmann, W. *The Structure and Properties of Water*; Oxford University Press: New York, 1969.

(56) Tabazadeh, A.; Turco, R. P.; Jacobson, M. Z. *J. Geophys. Res.* **1994**, *99*, 12897. An error in eq 6d was corrected to read: $\Omega = T°(z + {}^1/_2(T - T°)y)$ based upon eq 18d in: Clegg, S. L.; Brimblecombe, P. *J. Phys. Chem.* **1990**, *94*, 5369.

(57) Hanson, D.; Mauersberger, K. *J. Phys. Chem.* **1988**, *92*, 6167.

(58) Hanson, D. R. *Geophys. Res. Lett.* **1990**, *17*, 421.

(59) Koop, T.; Luo, B.; Biermann, U. M.; Crutzen, P. J.; Peter, T. *J. Phys. Chem. A* **1997**, *101*, 1117.

(60) Prenni, A. J.; Onasch, T. B.; Tisdale, R. T.; Siefert, R. L.; Tolbert, M. A. *J. Geophys. Res.*, submitted for publication.

(61) Ravishankara, A. R.; Hanson, D. R. *J. Geophys. Res.* **1996**, *101*, 3885.

(62) Henson, B. F.; Wilson, K. R.; Robinson, J. M. *Geophys. Res. Lett.* **1996**, *23*, 1021.

(63) Tsias, A.; Prenni, A. J.; Carslaw, K. S.; Onasch, T. B.; Luo, B. P.; Tolbert, M. A.; Peter, T. *Geophys. Res. Lett.* **1997**, *24*, 2303.

(64) Meilinger, S. K.; Koop, T.; Luo, B. P.; Huthwelker, T.; Carslaw, K. S.; Krieger, U.; Crutzen, P. J.; Peter, T. *Geophys. Res. Lett.* **1995**, *22*, 3031.

(65) Tabazadeh, A.; Toon, O. B.; Jensen, E. J. *Geophys. Res. Lett.* **1997**, *24*, 2007.

(66) Tabazadeh, A.; Jensen, E. J.; Toon, O. B. *J. Geophys. Res.* **1997**, *102*, 23845.

(67) Davy, J. G.; Somorjai, G. A. *J. Chem. Phys.* **1971**, *55*, 3624.

(68) Goodman, J.; Verma, S.; Pueschel, R. F.; Hamill, P.; Ferry, G. V.; Webster, D. *Geophys. Res. Lett.* **1997**, *24*, 615.

(69) Gao, R. S.; Fahey, D. W.; Salawitch, R. J.; Lloyd, S. A.; Anderson, D. E.; DeMajistre, R.; McElroy, C. T.; Woodbridge, E. L.; Wamsley, R. C.; Donnelly, S. G.; Del Negro, L. A.; Proffitt, M. H.; Stimpfle, R. M.; Kohn, D. W.; Kawa, S. R.; Lait, L. R.; Loewenstein, M.; Podolske, J. R.; Keim, E. R.; Dye, J. E.; Wilson, J. C.; Chan, K. R. *J. Geophys. Res.* **1997**, *102*, 3935.

(70) Adriani, A.; Deshler, T.; Di Donfrancesco, G.; Gobbi, G. P. *J. Geophys. Res.* **1995**, *100*, 25877.

(71) Koop, T.; Carslaw, K. S.; Peter, T. *Geophys. Res. Lett.* **1997**, *24*, 2199.

(72) Tabazadeh, A.; Turco, R. P. *J. Geophys. Res.* **1993**, *98*, 12727.

(73) Hanson, D. R. *J. Phys. Chem. B* **1997**, *101*, 4998.

(74) Tolbert, M. A.; Middlebrook, A. M. *J. Geophys. Res.* **1990**, *95*, 22423.

(75) Middlebrook, A. M.; Tolbert, M. A.; Drdla, K. *Geophys. Res. Lett.* **1996**, *23*, 2145.

(76) Peter, T.; Müller, R.; Crutzen, P. J.; Deshler, T. *Geophys. Res. Lett.* **1994**, *21*, 1331.

(77) Zondlo, M. A.; Barone, S. B.; Tolbert, M. A. *Geophys. Res. Lett.* **1997**, *24*, 1391.

(78) Abbatt, J. P. D. *Geophys. Res. Lett.* **1997**, *24*, 1479.

(79) Abbatt, J. P. D.; Beyer, K. D.; Fucaloro, A. F.; McMahon, J. R.; Wooldridge, P. J.; Zhang, R.; Molina, M. J. *J. Geophys. Res.* **1992**, *97*, 15819.

(80) Hanson, D. R.; Mauersberger, K. *J. Phys. Chem.* **1990**, *94*, 4700.

(81) Dominé, F.; Thibert, E.; Van Landeghem, F.; Silvente, E.; Wagnon, P. *Geophys. Res. Lett.* **1994**, *21*, 601.

(82) Burley, J. D.; Johnston, H. S. *Geophys. Res. Lett.* **1992**, *19*, 1363.

(83) Burley, J. D.; Johnston, H. S. *Geophys. Res. Lett.* **1992**, *19*, 1359.

(84) Toon, O. B.; Tolbert, M. A. *Nature* **1995**.

(85) Dye, J.; Baumgardner, D.; Gandrud, B. W.; Drdla, K.; Barr, K.; Fahey, D. W.; Del Negro, L. A.; Tabazadeh, A.; Jonsson, H. H.; Wilson, J. C.; Loewenstein, M.; Podolske, J. R.; Chan, K. R. *Geophys. Res. Lett.* **1996**, *23*, 1913.

(86) Shibata, T.; Iwasaka, Y.; Fujiwara, M.; Hayashi, M.; Nagatani, M.; Shiraishi, K.; Adachi, H.; Sakai, T.; Susumu, K.; Nakura, Y. *J. Geophys. Res.* **1997**, *102*, 10829.

(87) Carslaw, K. S.; Luo, B.; Peter, T. *Geophys. Res. Lett.* **1995**, *22*, 1877.